JOURNAL OF PROPULSION AND POWER
Vol. 25, No. 3, May–June 2009

Shock/Boundary-Layer/Tip-Clearance Interaction in a Transonic Rotor Blade

Roberto Biollo* and Ernesto Benini
University of Padova, 35131 Padova, Italy

DOI: 10.2514/1.39541

A newly designed rotor was modeled from the well-known radially stacked NASA rotor 37 by applying a three-dimensional shape to the original blade stacking line. A considerable curvature toward the direction of rotor rotation was given to the new blade. A three-dimensional numerical model, developed and validated using a commercial computational fluid dynamics Reynolds-averaged Navier–Stokes code, was adopted to predict the flowfield inside the new rotor. Steady-viscous-flow calculations were run at the design speed of the baseline configuration. Compared with rotor 37, the new rotor showed a higher efficiency, mainly due to a three-dimensional modification of the shock structure. At the outer span, the new rotor developed a blade-to-blade shock front located more downstream than in the baseline rotor, with a considerable impact on the flowfield near the casing. Computational fluid dynamics flow visualizations showed a less detrimental shock/boundary-layer/tip-clearance interaction at low-flow operating conditions, with a considerable reduction of the low-momentum-fluid region after the shock.

Nomenclature

E	=	adiabatic efficiency
k	=	specific heat capacity ratio
P	=	total pressure, Pa
T	=	total temperature, K
vax	=	axial velocity, m/s
vax, n	=	normalized axial velocity (vax/vp)
vp	=	blade-tip velocity, m/s

Subscripts

1	=	inlet section
4	=	outlet section

Introduction

TRANSONIC axial-flow compressor rotors are typically unshrouded and the blade-tip-gap region develops intense secondary flows. The pressure difference between the suction side and pressure side of the blade drives the fluid through the tip gap, inducing a jet that propagates into the main flow. The interaction between the jet and the main flow gives rise to a vortex, which develops into the passage channel. The complex flow structures arising from the interaction between these tip-clearance flows, the casing boundary layer, and the passage shock have detrimental effects on the overall rotor performance, inducing aerodynamic losses [1], blockage [2], and instabilities [3].

Many research efforts have been spent to better understand the aerodynamic phenomena that take place in the tip endwall region of a transonic compressor rotor. It was observed that the interaction between the shock and the tip-clearance vortex plays an important role in determining the overall rotor performance. The shock/vortex interaction, in particular, is believed to be one of the main stall triggers in transonic compressors. Interacting with the shock, the vortex is subjected to a sudden and strong deceleration; depending on the intensity of the interaction, vortex breakdown can occur, inducing compressor instability [3].

Received 3 July 2008; revision received 5 December 2008; accepted for publication 5 December 2008.

*Researcher, Department of Mechanical Engineering, Via Venezia 1; roberto.biollo@unipd.it.

The use of swept and leaned blades (i.e., the use of curved blades) can considerably influence the internal flow structures in transonic rotors (*sweep* is defined as the movement of blade sections along the local chord line, and *lean* is defined as the change in the perpendicular direction). Sweep and lean can have effects on the blade loading and, consequently, on the tip-clearance flows; further, a significant impact on the three-dimensional shock structure can be induced. Consequently, the tip endwall flowfield and, in particular, the shock/tip-clearance vortex interaction can be significantly influenced using the blade-curvature concept.

It was observed, for instance, that the application of forward sweep (i.e., the upstream movement, at the outer span, of blade sections along the local chord direction) on a conventional transonic compressor rotor moves the shock downstream near the casing, as a consequence of the so-called endwall effect [4]. It seems that a shock located more downstream at the outer span region helps to delay the vortex breakdown, leading to a better stability. Actually, many numerical and experimental studies showed a better stability in forward-swept rotors than in conventional radially stacked rotors [4–7]. An explanation for that was given in [7] and is briefly summarized in the following. Vortex breakdown occurs when the relative total pressure in vortex core is lower than the static pressure downstream of the shock. After reaching a local minimum, the relative total pressure inside the vortex core is increased by a mixing process between the low-momentum core, the higher-momentum outer parts of the vortex, and the main flow. Whether it remains possible for the vortex to get past the passage shock depends on the axial distance that is available for this reenergization.

In addition, sweep influences the loading on the blade near the walls [8]. In particular, forward sweep can reduce the blade loading in the front area of the tip region, in which the loading rapidly falls down to zero (no blade) as one moves radially from the tip to a lower span. This helps to reduce the sensitivity to changes in incidence and the intensity of the tip-leakage flows in this area.

The influence of lean in transonic compressor rotors is not extensively described in the literature. However, some research carried out using optimization techniques showed appreciable improvements in the overall rotor performance when blades properly curved in the tangential direction were used. In particular, the possibility to increase the overall rotor efficiency by skewing the blade toward the direction of rotor rotation was observed [9,10]. Similar results were recently obtained by [11,12]. It seems that the better performance is associated with a favorable modification of the three-dimensional shock structure, leading to a reduction of the related aerodynamic losses.

In previous investigations [13,14], the authors numerically studied the impact of a large number of new stacking lines on the

aerodynamic behavior of a transonic compressor rotor. The possibility to improve the overall efficiency of a baseline radially stacked configuration by giving the blade a proper curvature toward the direction of rotor rotation was confirmed. In this work, the impact of such a blade shape on the tip endwall flowfield was investigated. With this aim, a novel transonic compressor rotor was modeled starting from the well-known radially stacked NASA rotor 37 by giving the blade the promising spatial curvature. The study was numerically carried out. A 3-D numerical model for transonic compressor rotors was developed and validated using a commercial computational fluid dynamics (CFD) Reynolds-averaged Navier–Stokes (RANS) code. At first, the overall performance of the new rotor was calculated and compared with that of the baseline configuration. Then the impact of the applied blade curvature on the tip endwall flowfield was analyzed in detail.

Investigated Rotor Geometry

Figure 1 shows the meridional view of the NASA rotor 37, the baseline radially stacked transonic compressor rotor from which the rotor analyzed in this work was derived. Rotor 37 was originally designed and tested at the NASA Lewis Research Center by Reid and Moore [15,16] and then investigated by many other researchers [17–22]. Representative values for this rotor are given in Table 1.

The new rotor was obtained from the rotor 37 geometry by changing the three-dimensional shape of the original stacking line, as schematically shown in Figs. 2 and 3. The shape of the new stacking line comes from previous investigations by the authors. In [13,14], the impact of stacking line shape on rotor 37 performance was systematically investigated. As schematically shown in Fig. 4, in such works the radial stacking line of rotor 37 (the solid vertical line) was modified by moving three control points (located on 33, 67, and 100% span from the hub and signed as black circles) on predefined positions (the x-marked locations). This was done in the meridional plane and in the circumferential plane separately. The x-marked locations were defined so that the new blades were sufficiently different from the original one, to have a clear understanding of the induced aerodynamic effects without leading to unreasonable end excessively strange blades. Considering all possible combinations, 26 new blades curved in the meridional plane and 26 new blades curved in the circumferential plane were obtained and numerically evaluated from the aerodynamic point of view (in Fig. 4, only some new stacking lines are shown). The higher overall efficiencies (over one percentage point higher than that of the baseline configuration around the design operating condition) were given by blades curved toward the direction of rotor rotation. The circumferential shape shown in Fig. 2 actually corresponds to the most promising stacking line shape (in terms of efficiency) among those evaluated in such works (cf. "leaned rotor" in [13] and "forward leaned 1" in [14]).

On the other side, mechanical analyses showed a detrimental impact on blade structural behavior when such circumferential curvature was applied [24]. In particular, static linear simulations showed an intensification of blade structural stresses as a consequence of strong bending loads arising from the action of centrifugal force. Figure 5 gives the computed von Mises stress distribution on the blade pressure side due to the centrifugal load in the case of the baseline blade of rotor 37 (Fig. 5a), the blade obtained by giving the baseline blade only the circumferential curvature shown in Fig. 2 (Fig. 5b), and the blade obtained by giving both the circumferential and meridional curvatures shown in Fig. 2 (Fig. 5c). A fixed constraint was imposed at the blade hub section. The negative effects induced by the application of the circumferential curvature are clearly visible (cf. Figs. 5a and 5b). In general, this can be simply explained as follows. If the blade is radially stacked, the centrifugal load gives rise to a tensile stress only, but if the blade is noticeably curved, the centrifugal load gives rise to both a tensile stress and a bending stress. In transonic compressor rotors, the centrifugal load is strong (due to the high blade-tip velocity) and considerable bending stresses can arise, leading to an amplification of overall structural stresses.

The addition of the meridional curvature shown in Fig. 2 can be considered as a first attempt to verify the possibility of reducing the negative structural effects due to the application of such a

Table 1 Representative values for rotor 37 [23]

Number of rotor blades	36
Rotor inlet hub-to-tip-diameter ratio	0.7
Rotor blade aspect ratio	1.19
Tip solidity	1.288
Design wheel speed, rad/s	1800
Tip speed, m/s	454.136
Running tip clearance, mm	0.356
Design rotor total pressure ratio	2.106
Design rotor adiabatic efficiency	0.877
Measured choking mass flow rate, kg/s	20.93

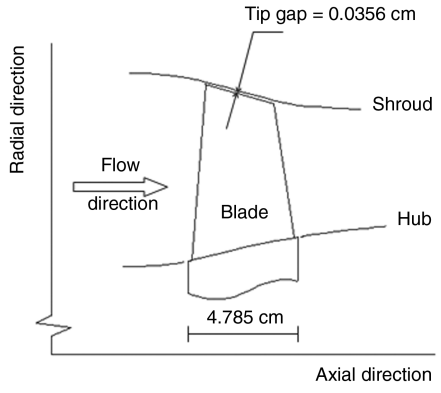

Fig. 1 Meridional view of NASA rotor 37.

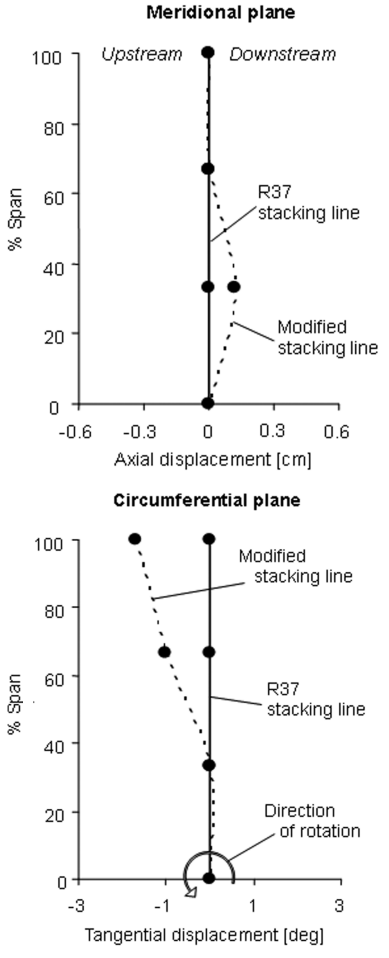

Fig. 2 New stacking line.

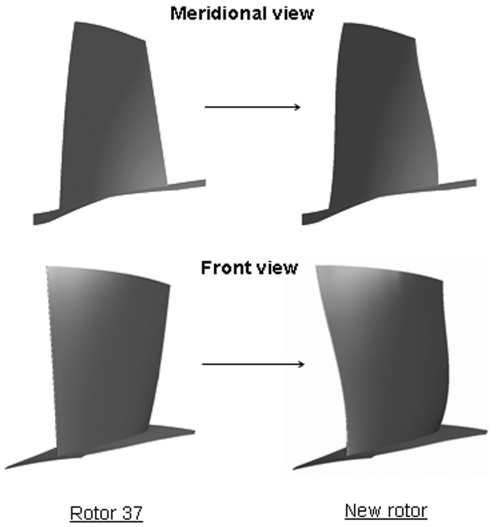

Fig. 3 Baseline blade and new blade.

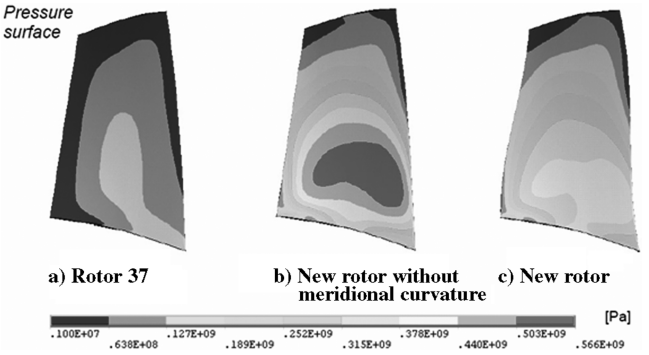

Fig. 5 Von Mises stress distribution due to wheel speed (1800 rad/s) (ANSYS Structural).

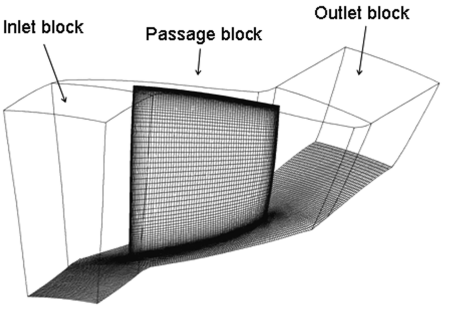

Fig. 6 Computational grid for NASA rotor 37 (ANSYS TurboGrid).

circumferential curvature without compromising the induced aerodynamic benefits. Substantially, the blade was slightly axially swept at the inner half-span, where the applied circumferential curvature does not act. It was swept downstream because such a sweep seems to be promising from the structural point of view. Figure 5 shows the structural impact of the applied meridional curvature (cf. Figs. 5b and 5c).

Numerical Model and Validation

The aerodynamic behavior of the new rotor was compared with that of the baseline configuration. The flowfield inside each rotor was simulated by means of a commercial CFD package (ANSYS CFX), in which the 3-D Reynolds-averaged Navier–Stokes equations were solved using the finite volume method. Steady-state simulations were carried out using the k-ε turbulence model [25], along with the scalable wall functions.

A multiblock structured grid of about 1 million cells was adopted to discretize the computational domain (Fig. 6). The computational domain is relative to a single blade passage. An H-type grid was used for both the inlet and the outlet blocks; a composite J/O-type grid was instead used for the passage block, to have a low grid skewness and to well solve the boundary layer around the blade. Grid points are distributed as follows. Both the inlet and the outlet blocks have 29 points streamwise and 49 points blade to blade. The passage block has 101 points streamwise and 30 points from the blade to the periodic boundary, with 10 points inside the O-grid. From the hub to the casing there are 117 points. To make the code able to accurately solve the wall boundary layer formed by the relative motion between the overtip-leakage flow and the casing, which seems to have a considerable impact on the development of the tip-clearance flows [26], the tip-clearance gap was modeled using 20 radial grid points clustered toward the casing.

Calculations were run at the design speed of the baseline configuration (1800 rad/s). The speed line of both baseline and new rotors was calculated by fixing the total pressure, total temperature, and absolute flow angle at the inflow boundary and varying the static pressure at the outflow boundary; the static pressure was imposed at the outflow as a mass-averaged value (the boundary-pressure profile is an implicit result of the computation, calculated using the radial equilibrium condition). The model was validated against the NASA rotor 37 experimental data available in literature. A lot of them are referred to as stations 1 and 4 (Fig. 7); these measurement stations correspond to the inflow and outflow boundaries of the computational domain. With the aim to reproduce the experimental conditions at station 1, the inflow boundary conditions of the model were fixed at standard values ($P_1 = 101,330$ Pa and

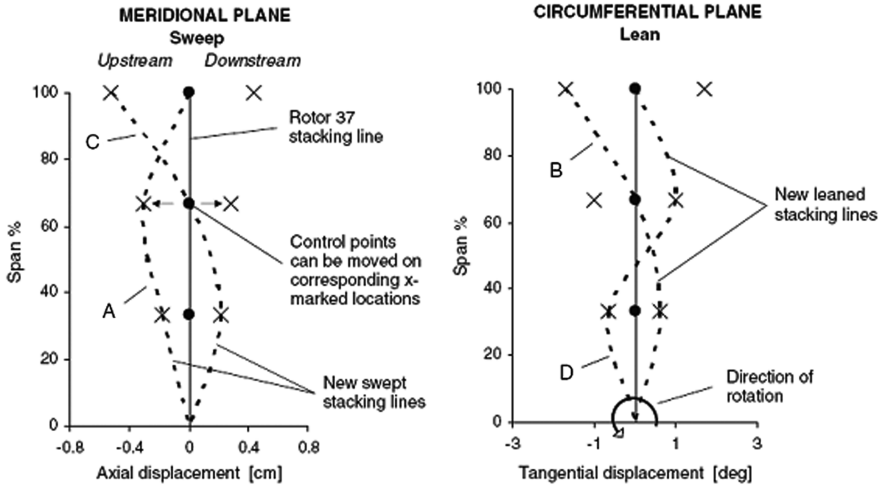

Fig. 4 Systematic modification of stacking line [13].

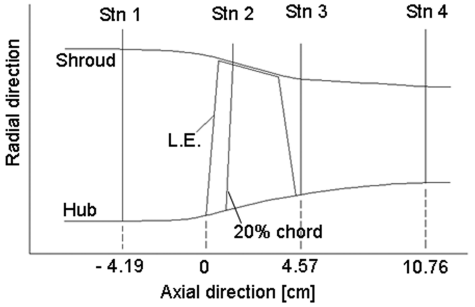

Fig. 7 Measurement stations within NASA rotor 37.

$T_1 = 288.15$ K). Periodic boundary conditions were applied on the lateral faces of the computational domain. All of the walls were treated as smooth and adiabatic. For each simulation, the convergence criterion was established when normalized rms residuals were less than 1×10^{-6}. The lower mass flow operating point in the calculated speed lines represents the last point for which the steady-state model implemented was able to converge.

Figure 8 compares the computed and experimental rotor speed lines of the baseline configuration in the form of total pressure ratio P_4/P_1 and adiabatic efficiency E

$$E = \frac{(P_4/P_1)^{\frac{k-1}{k}} - 1}{(T_4/T_1) - 1}$$

against the normalized mass flow rate. The calculated and measured mass flows were normalized using the corresponding mass flow at the choking condition. Note that the data for the choking condition were not included in the figure because the related total pressure ratio is out of the scale range. The predicted choking mass flow is 20.96 kg/s, and the experimental value is 20.93 ± 0.14 kg/s. The rotor speed line was well predicted at the low-flow operating conditions. Some disagreements can instead be observed around the peak efficiency zone, in which both the total pressure ratio and the adiabatic efficiency are out of the measurement uncertainties. The reasons for that were not well understood, especially because the steady-state RANS with the k-ε turbulence model should be accurate only around the peak efficiency condition and not near stall, where the unsteadiness of the flow and the high turbulence level and flow separations are not properly covered by the model. In any case, Fig. 8 is in agreement with Fig. 9, which shows the calculated and measured spanwise performance profiles at the 98 and 93% normalized mass flow rates (circumferentially-mass-averaged values). The 98% normalized mass flow rate represents a working point close to the

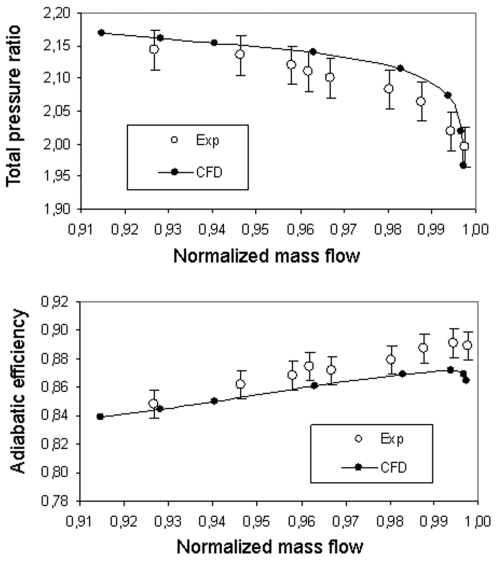

Fig. 8 Measured [23] and calculated rotor 37 speed lines.

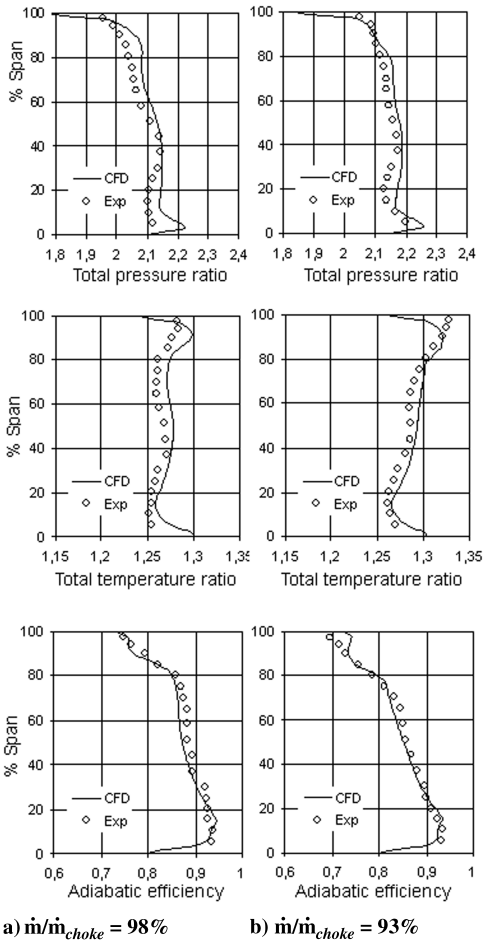

Fig. 9 Spanwise distributions of flow properties at station 4 (experimental data from [23]).

design point of rotor 37. The comparison between CFD and experimental data is better at the 93% choking flow condition than at 98%. At 98%, some differences can be observed for both the total pressure ratio and the total temperature ratio at the outer and inner span levels. Despite that, the computed efficiency profile is relatively good compared with measured data: that is, the profile shape was well predicted. This is simply due to the expression of adiabatic efficiency, which leads to a compensation effect when both the total pressure ratio and the total temperature ratio are overpredicted.

The model showed a suitable capability to predict the local flow features that characterize a transonic compressor rotor. Figure 10 shows the blade-to-blade view of the shock structure near the leading edge at 70% span at a low-flow operating condition. As can be seen, calculations are in quite good agreement with measurements. Figure 11 compares the blade-to-blade view of computed and experimental normalized axial velocity component (vax, n, normalized using the blade-tip velocity $vp = 454$ m/s) at 95% span and 98% of choking mass flow. Despite the well-known difficulty to correctly predict the tip-clearance vortex pattern and its interaction with the shock front (probably due to the inability of current turbulence models to well calculate the development of casing boundary layer), predictions can be considered satisfactory.

Results

Figure 12 compares the computed speed line of the new rotor to that of the baseline configuration. For each rotor, the calculated mass flows were normalized using the corresponding computed mass flow at the choking condition (the new rotor gave a choking mass flow of 20.88 kg/s against 20.96 kg/s of rotor 37). As in Fig. 8, the given speed lines do not contain the data for the choking condition. With respect to the baseline configuration, the new rotor gave a higher

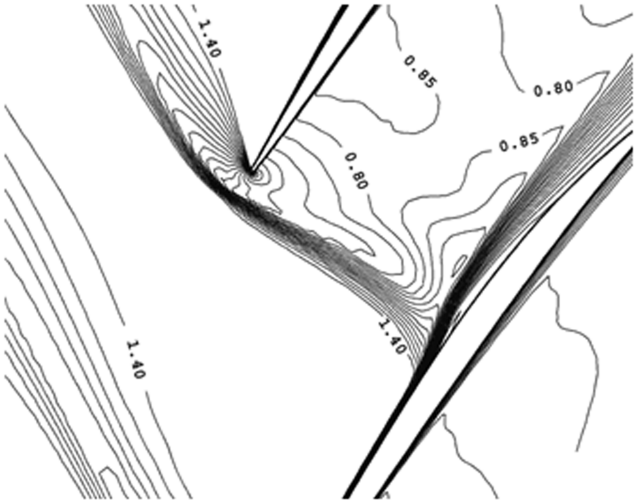

a) CFD results

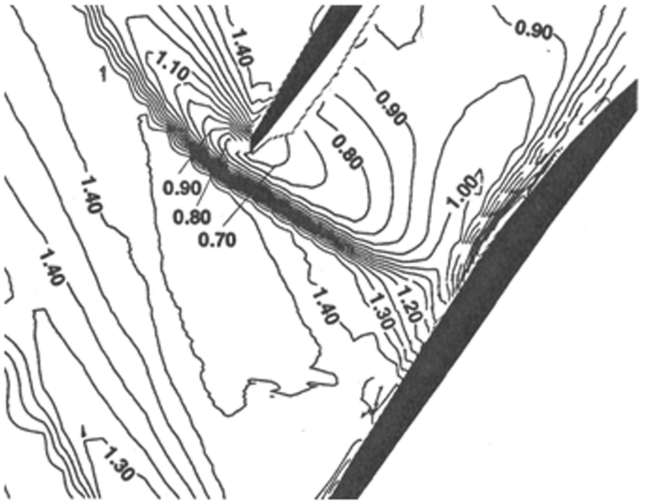

b) Experimental data (extracted from [2])

Fig. 10 Blade-to-blade relative Mach number distribution near the leading edge at 70% span and $\dot{m}/\dot{m}_{\text{choke}} = 93\%$.

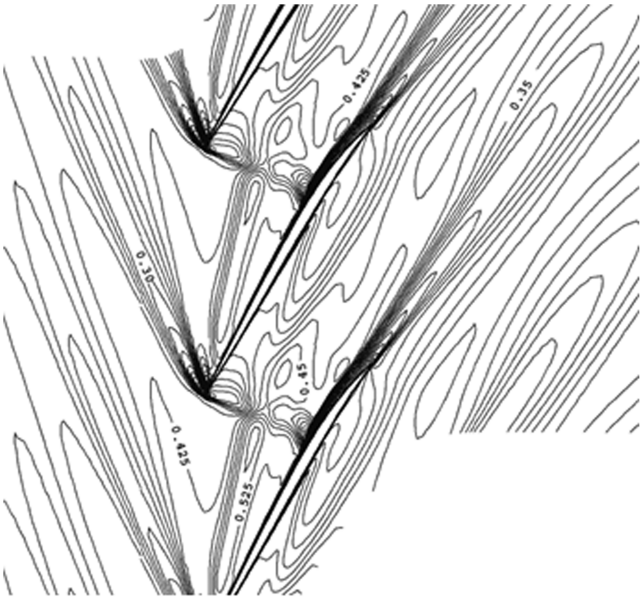

a) CFD results

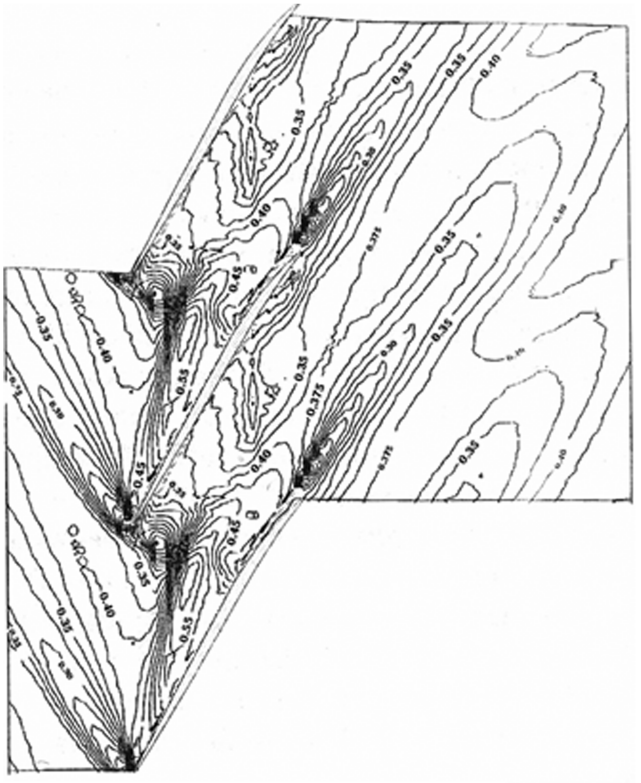

b) Experimental data (extracted from [20])

Fig. 11 Contours of normalized axial velocity component at 95% span and $\dot{m}/\dot{m}_{\text{choke}} = 98\%$.

overall efficiency and a similar total pressure ratio. The calculated efficiency increment is of about 0.8 percentage points around the peak efficiency condition.

It is clear that such an increment in efficiency can be questionable, because the validation of the model is not quite accurate at the peak efficiency point and the model might not cover all the important flow features appropriately. However, it is interesting to understand the reasons for which the model computed such improvement. With this aim, the flowfields of the two rotors were analyzed and compared at about 98% of the choking mass flow (which is, as aforementioned, a working point close to the design point of the baseline rotor). In addition, a detailed flow analysis was carried out at about 93% of the choking mass flow to understand the reasons for the lower working range given by the new rotor with respect to the baseline configuration. Figure 12 shows the operating points analyzed.

Numerical flow visualizations showed an unusual flow pattern near the leading edge inside the new rotor, especially at the outer span region. Considering 98% of the choking mass flow in the new rotor (whereas in the baseline rotor, the flow moves around the leading edge without any evident spanwise velocity component), the flow clearly deviates radially inward (Fig. 13a). This leads to a different local flow deviation and influences both the three-dimensional shock structure and the blade loading. In fact, with respect to the baseline rotor, the new rotor at the outer span region showed a different blade-to-blade shock front (Fig. 13b) and a lower blade loading at the leading edge (Fig. 13c). As far as the shock is concerned, Figs. 13b and 13c show that the new rotor has replaced a single shock with a double-shock system, with the first wave more inclined downstream than the single one of the baseline configuration. Such a solution can help to reduce the aerodynamic losses associated with the shock [6], laying the basis for a more efficient local flow diffusion. This was confirmed by Fig. 14, which shows a significant reduction of total temperature ratio T_4/T_1 above 50% span, with a positive impact on the efficiency between 50 and 85% span.

Figure 15 shows the relative Mach number distribution at the blade-tip span location (about 99.4% span) for 98% of the choking mass flow. The black dashed line points out the tip-clearance vortex core (or primary vortex core). In the baseline rotor, the vortex starts at the leading edge; in the new rotor, it starts at about 10% chord, due to

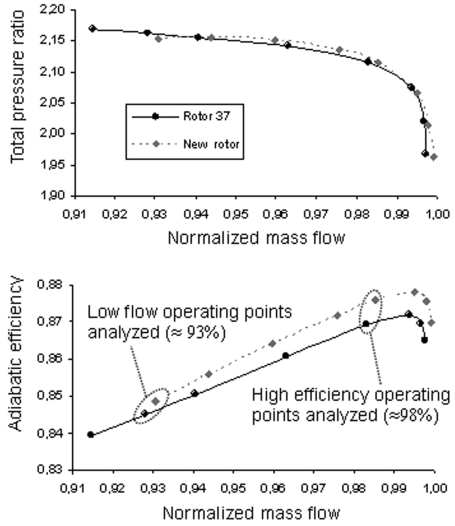

Fig. 12 Rotor 37 and new rotor calculated speed lines.

the lower blade loading at the leading edge. Further, the shock/tip-clearance vortex interaction point is located more downstream in the new rotor, as a consequence of the different shock configuration. These new flow features, however, did not have considerable effects on the local efficiency. As shown in Fig. 14, the efficiency is comparable with that of rotor 37 near the casing.

Figure 16 shows the relative Mach number distribution at the blade tip for 93% of the choking mass flow (see Fig. 12). At this operating condition, the tip-clearance vortex starts at the leading edge in both rotors, but the shock front in the new rotor remains located more downstream (still attached to the blade leading edge). This led to a higher distance between the vortex start point and the shock/vortex interaction point. As said in the Introduction, this flow configuration can lead to a less detrimental shock/vortex interaction. Actually, the new rotor showed a low-momentum region after the shock to be significantly less unfavorable.

Figure 17 shows some three-dimensional streamlines released at midheight in the tip-clearance gap, along with the relative Mach number distributions at blade-tip span and 96% span. The tip-clearance vortex (or primary vortex) is clearly visible. A secondary

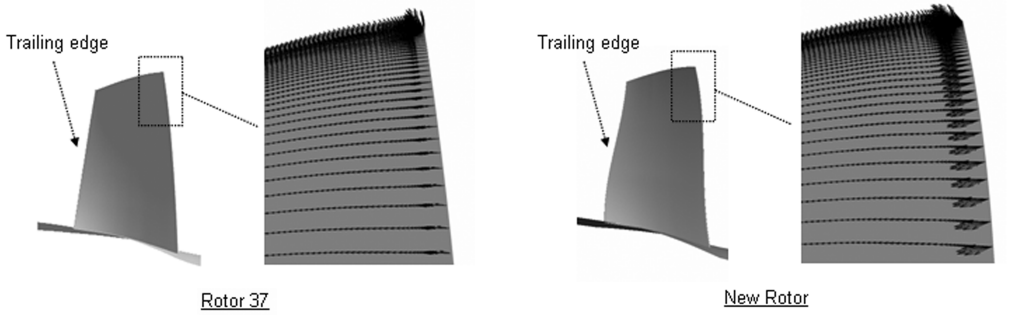

a) Relative velocity vectors near pressure side

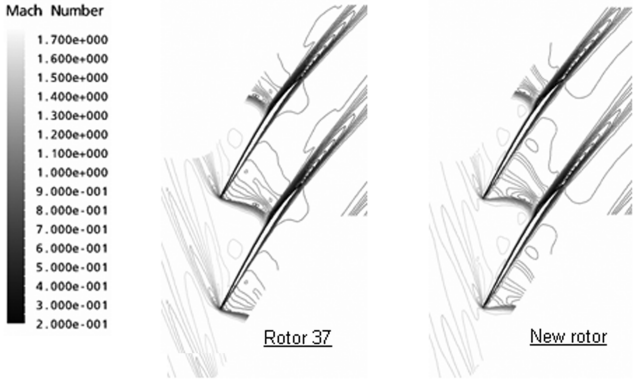

b) Relative Mach number contours – 85% span

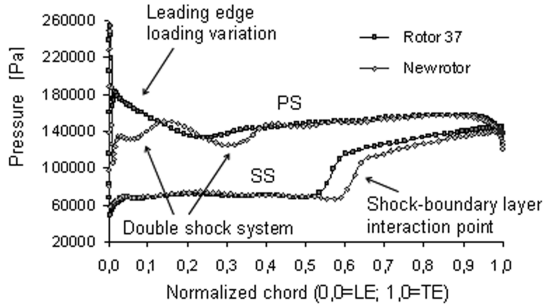

c) Blade loading – 85% span

Fig. 13 Rotor 37 and new rotor comparisons at $\dot{m}/\dot{m}_{\text{choke}} \approx 98\%$.

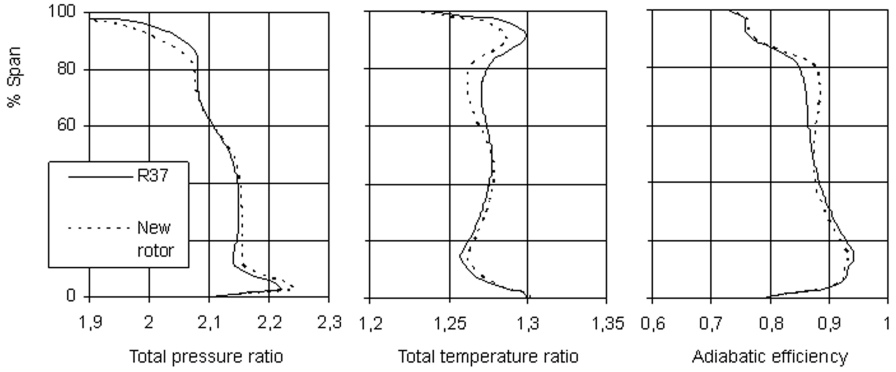

Fig. 14 Spanwise performance profiles at the outlet at $\dot{m}/\dot{m}_{\text{choke}} \approx 98\%$.

vortex, arising after the shock, can also be seen in both rotors. Because the streamlines are released from the tip-clearance gap, the two vortices arise from the pressure difference between the pressure side and the suction side of the blade. Really, it the case of the secondary vortex, it was observed that it is also formed from fluid coming from the blade suction-side boundary layer, which moves radially outward after the shock.

Compared with the new rotor, the low-momentum region after the shock developed by the baseline rotor is considerably wider in the spanwise direction. As shown in Fig. 17, at 96% span it is still visible inside rotor 37, whereas it does not appear in the new rotor. It is also interesting to observe the difference in the blade wake development. Mainly due to a more detrimental shock/boundary-layer interaction, the baseline rotor showed a wider and deeper blade wake at the outer span with respect to the new rotor.

On the whole, at 93% of the choking mass flow, the new rotor blade showed a better aerodynamic behavior at the tip endwall region, compared with the baseline one. This is also confirmed by the higher efficiency shown toward the casing (Fig. 18). Because the rotor stability seems to be directly linked to the flowfield near the casing (as said in the Introduction, the shock/vortex interaction is

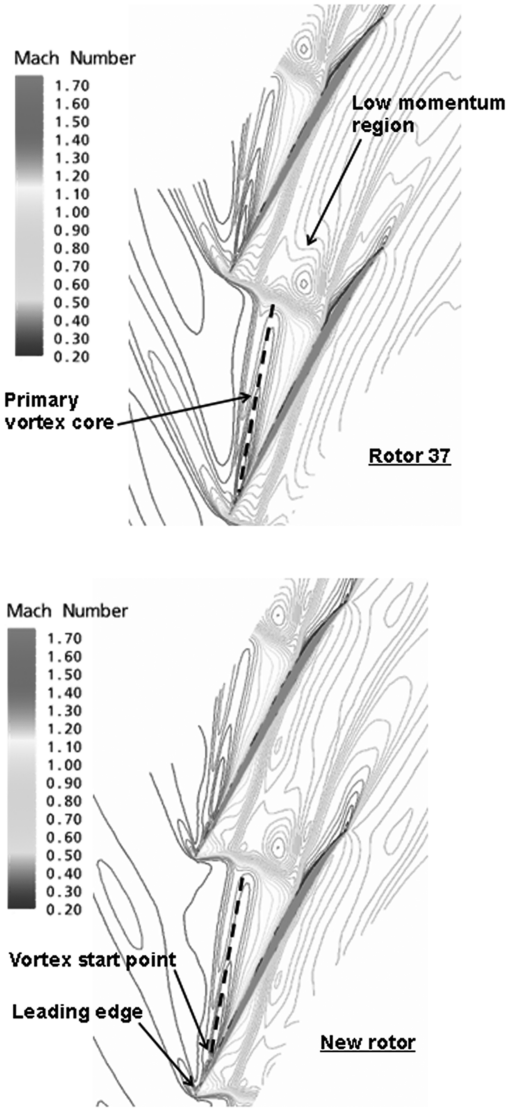

Fig. 15 Blade-to-blade relative Mach number distribution. Blade-tip span at $\dot{m}/\dot{m}_{\text{choke}} \approx 98\%$.

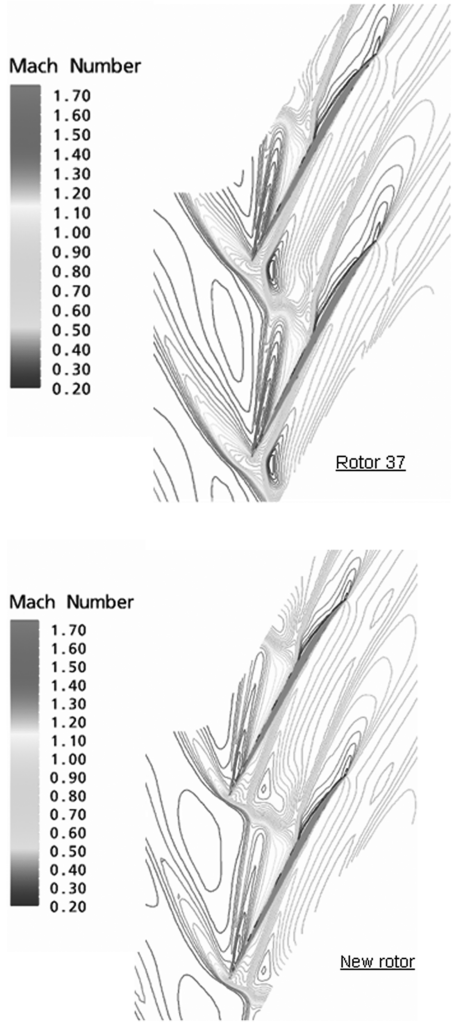

Fig. 16 Blade-to-blade relative Mach number distribution. Blade-tip span at $\dot{m}/\dot{m}_{\text{choke}} = 93\%$.

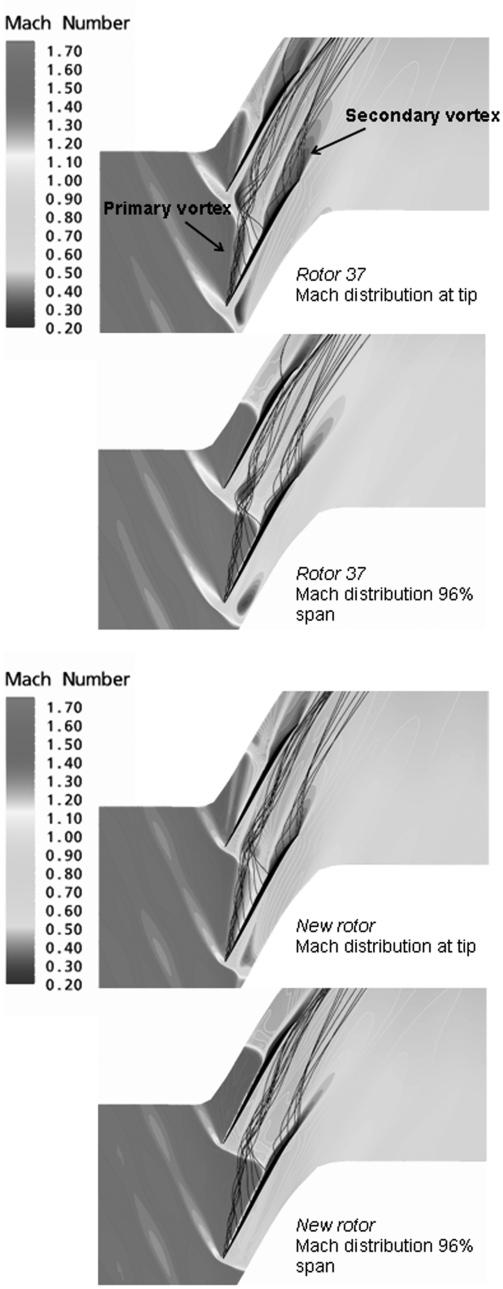

Fig. 17 Flow visualizations at $\dot{m}/\dot{m}_{\text{choke}} = 93\%$.

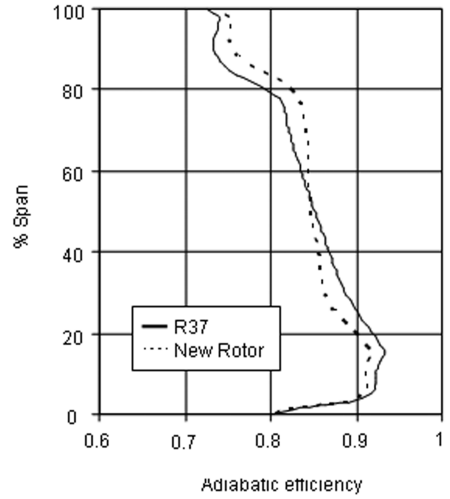

Fig. 18 Spanwise profile of efficiency at the outlet at $\dot{m}/\dot{m}_{\text{choke}} = 93\%$.

believed to be one of the main stall triggers in transonic compressor rotors), the less detrimental tip endwall flowfield of the new rotor might lead to a higher operating range. In [7], for instance, a swept version of a radially stacked transonic compressor rotor experimentally showed a higher stall margin than the original one as a consequence of a higher distance from the vortex appearance point to the intersection with the passage shock, which led to a less harmful tip endwall flowfield. Here, instead, the new rotor seems to have a lower operating range with respect to the original one (Fig. 12). A steady-state model, however, could be not suitable to provide information about rotor stability at low-flow working points, due to the high unsteadiness of the flowfield near stall. As aforementioned, the lower mass flow operating point in the calculated speed lines represents the last point for which the model implemented was able to converge. For lower normalized mass flow rates, the solver diverged or, more generally, was not able to give a converging solution. In any case, the difficult of a numerical steady calculation to converge cannot be directly identified with a real stall phenomenon: it could be due to a numerical reason. This was confirmed by the following.

Further simulations were carried out using the more accurate shear stress transport (SST) k-ω turbulence model [27], instead of the more traditional k-ε turbulence model. The SST k-ω model was designed to give highly accurate predictions of the onset and the amount of flow separation under adverse pressure gradients. A finer grid of about 1,200,000 cells was used to have a near-wall grid resolution of at least $y^+ < 1$, needed to guarantee a strict low-Reynolds-number model implementation at the walls. Automatic near-wall treatment, which switches from the low-Reynolds-number near-wall formulation to the scalable wall functions, as the mesh is not sufficiently refined, was also adopted.

The SST k-ω model was initially discarded because it was unable to provide accurate results in terms of overall performance. The overall efficiency of rotor 37, for instance, was significantly underestimated, with an error of about 3.5 percentage points at the peak efficiency condition (Fig. 19). Nevertheless, simulations using this turbulence model were all conducted the same, and calculations again showed a better aerodynamic behavior of the new rotor compared with that of rotor 37. Similarly to the k-ε turbulence model, in the case of the new rotor, the SST k-ω model gave a higher efficiency [about 1.1 percentage points at the peak efficiency condition (see Fig. 19)] and a less detrimental flowfield near the casing toward the stall (Figs. 20 and 21). Even though the flowfields calculated by the two turbulence models do not match well (compare Fig. 16 with Fig. 21 and Fig. 17 with Fig. 20), the predicted flow changes due to the new blade curvature are similar. In the case of the new rotor, both models calculated a blade-to-blade shock structure less detached from the leading edge and located more downstream, a less detrimental shock/boundary-layer interaction at the blade suction side, and a vortex less distorted after crossing through the shock. On the other side, differently from the k-ε model, the SST k-ω model gave a higher operating range in the case of the new rotor, in agreement with the more stable flowfield near the casing. This corroborated the preceding observations on the use of a steady-state model to predict the rotor stall point. The two models showed similar improvements on the peripheral flowfield of the new rotor, but different stall points, probably due to a different numerical stability

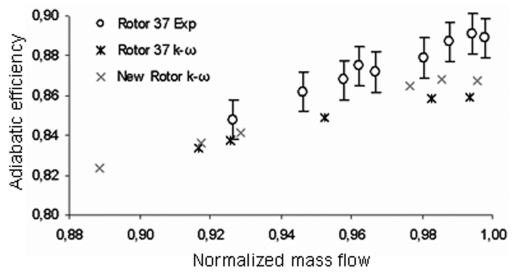

Fig. 19 Rotor 37 and new rotor operating points (experimental data from [23]).

toward the low-flow operating conditions. Therefore, as previously remarked, the lower operating range shown by the k-ε model in the case of the new rotor cannot be directly associated with a flow instability, and the possibility to delay the rotor stall to a lower mass flow using a blade curvature as that considered here (or similar) cannot be neglected.

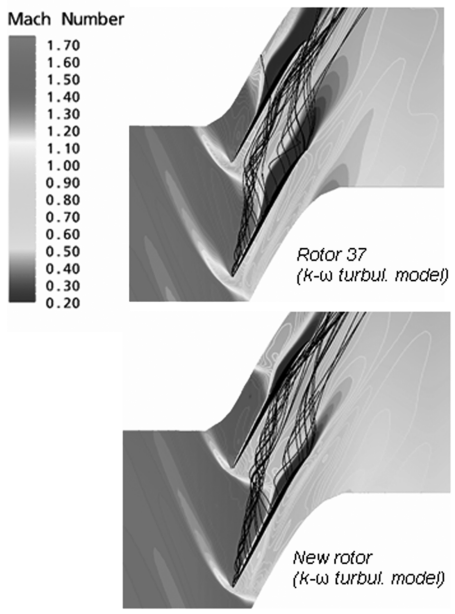

Fig. 20 Mach number distribution (96% span) and streamlines from the tip gap at $\dot{m}/\dot{m}_{\text{choke}} \approx 93\%$.

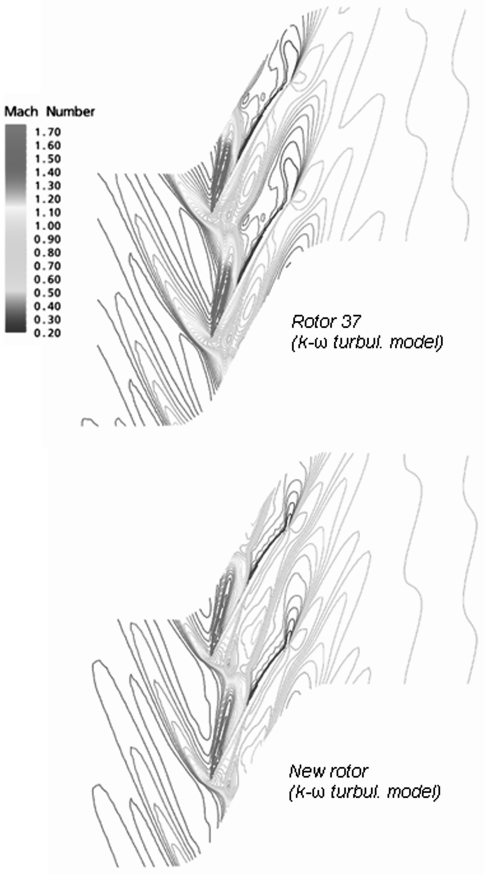

Fig. 21 Blade-to-blade relative Mach number distribution. Blade-tip span at $\dot{m}/\dot{m}_{\text{choke}} \approx 93\%$.

Conclusions

A novel transonic compressor rotor was modeled starting from the well-known NASA rotor 37 by changing the three-dimensional shape of the original stacking line. A considerable curvature toward the direction of rotor rotation was given to the new blade. The aerodynamic impact of the new blade on the tip endwall flowfield was evaluated and compared with that of the baseline blade using a 3-D CFD model. The model was developed using a commercial RANS code and validated using the existing rotor 37 experimental data.

With respect to the baseline rotor, the new rotor showed a higher efficiency (about 0.8 percentage points at the peak efficiency condition) and a similar total pressure ratio. The choking mass flow was not significantly influenced by the new blade design.

The efficiency increment in the new rotor can be associated with a more favorable shock structure at the outer half-span (mainly induced by an unusual flow pattern near the blade leading edge). The new shock structure reduced the shock losses and had also a positive impact on the tip endwall flowfield. A less detrimental low-momentum-fluid region after the shock was observed at the low-flow operating conditions, as well as a less harmful shock/blade boundary-layer interaction.

References

[1] Fritsch, G., Hoeger, M., Blaha, C., and Bauer, D., "Viscous Three-Dimensional Simulation of Transonic Compressor Stage on Parallel Hardware," *Journal of Propulsion and Power*, Vol. 16, No. 3, 2000, pp. 388–396. doi:10.2514/2.5600

[2] Suder, K. L., "Blockage Development in a Transonic, Axial Compressor Rotor," *Journal of Turbomachinery*, Vol. 120, July 1998, pp. 465–476.

[3] Hofmann, W., and Ballmann, J., "Tip Clearance Vortex Development and Shock-Vortex Interaction in a Transonic Axial Compressor Rotor," AIAA Paper 2002-0083, 2002.

[4] Hah, C., Puterbaugh, S. L., and Wadia, A. R., "Control of Shock Structure and Secondary Flow Field Inside Transonic Compressor Rotors Through Aerodynamic Sweep," American Society of Mechanical Engineers Paper 98-GT-561, 1998.

[5] Wadia, A. R., Szucs, P. N., and Crall, D. W., "Inner Workings of Aerodynamic Sweep," *Journal of Turbomachinery*, Vol. 120, 1998, pp. 671–682.

[6] Denton, J. D., and Xu, L., "The Effects of Lean and Sweep on Transonic Fan Performance," American Society of Mechanical Engineers Paper GT-2002-30327, 2002.

[7] Kablitz, S., Hennecke, D. K., Passrucker, H., and Engber, M., "Experimental Analysis of the Influence of Sweep on Tip Leakage Vortex Structure on an Axial Transonic Compressor Stage," International Society for Air Breathing Engines Paper 2003-1226, 2003.

[8] Denton, J. D., and Xu, L., "The Exploitation of Three-Dimensional Flow in Turbomachinery Design," *Proceedings of the Institution of Mechanical Engineers Part C, Mechanical Engineering Science*, Vol. 213, No. 2, 1999, pp. 125–137. doi:10.1243/0954409991531083

[9] Ahn, C. S., and Kim, K. Y., "Aerodynamic-Design Optimization of an Axial Compressor Rotor," American Society of Mechanical Engineers Paper GT-2002-30445, 2002.

[10] Benini, E., "Three-Dimensional Multi-Objective Design Optimization of a Transonic Compressor Rotor," *Journal of Propulsion and Power*, Vol. 20, No. 3, 2004, pp. 559–565. doi:10.2514/1.2703

[11] Jang, C. M., Samad, A., and Kim, K. Y., "Optimal Design of Swept, Leaned and Skewed Blades in a Transonic Axial Compressor," American Society of Mechanical Engineers Paper GT2006-90384, 2006.

[12] Yi, W., Huang, H., and Han, W., "Design Optimization of Transonic Compressor Rotor using CFD and Genetic Algorithm," American Society of Mechanical Engineers Paper GT2006-90155, 2006.

[13] Benini, E., and Biollo, R., "Aerodynamics of Swept and Leaned Transonic Compressor-Rotors," *Applied Energy*, Vol. 84, No. 10, Oct. 2007, pp. 1012–1027. doi:10.1016/j.apenergy.2007.03.003

[14] Biollo, R., and Benini, E., "Systematic Investigation on Swept and Leaned Transonic Compressor Rotor Blades," *7th European*

Turbomachinery Conference, National Technical Univ. of Athens, Athens, 5–9 Mar. 2007, pp. 205–214.

[15] Reid, L., and Moore, R. D., "Design and Overall Performance of Four Highly Loaded, High-Speed Inlet Stages for an Advanced High-Pressure-Ratio Core Compressor," NASA TP 1337, 1978.

[16] Reid, L., and Moore, R. D., "Experimental Study of Low Aspect Ratio Compressor Blading," American Society of Mechanical Engineers Paper 80-GT-6, 1980.

[17] Hah, C., and Reid, L., "A Viscous Flow Study of Shock-Boundary Layer Interaction, Radial Transport and Wake Development in a Transonic Compressor," *Journal of Turbomachinery*, Vol. 114, July 1992, pp. 538–547. doi:10.1115/1.2929177

[18] Suder, K. L., and Celestina, M. L., "Experimental and Computational Investigation of the Tip Clearance Flow in a Transonic Axial Compressor Rotor," *Journal of Turbomachinery*, Vol. 118, Apr. 1996, pp. 218–229.

[19] Hah, C., and Loellbach, J., "Development of Hub Corner Stall and Its Influence on the Performance of Axial Compressor Blade Rows," American Society of Mechanical Engineers Paper 97-GT-42, 1997.

[20] Chima, R. V., "Calculation of Tip Clearance Effects in a Transonic Compressor Rotor," *Journal of Turbomachinery*, Vol. 120, Jan. 1998, pp. 131–140.

[21] Gerolymos, G. A., and Vallet, I., "Tip-Clearance and Secondary Flows in a Transonic Compressor Rotor," *Journal of Turbomachinery*, Vol. 121, Oct. 1999, pp. 751–762.

[22] Yamada, K., Furukawa, M., Nakano, T., Inoue, M., and Funazaki, K., "Unsteady Three-Dimensional Flow Phenomena Due to Breakdown of Tip Leakage Vortex in a Transonic Axial Compressor Rotor," American Society of Mechanical Engineers Paper GT2004-53745, 2004.

[23] Dunham, J., "CFD Validation for Propulsion System Components," AGARD Rept. 355, Neuilly-sur-Seine, France, May 1998.

[24] Biollo, R., and Benini, E., "Impact of Aerodynamic Sweep and Lean on the Structural Behaviour of a Transonic Rotor Blade," European Turbine Network, Paper S2 T2/2, Oct. 2006.

[25] Launder, B., and Spalding, D., "The Numerical Computation of Turbulent Flow," *Computer Methods in Applied Mechanics and Engineering*, Vol. 3, No. 2, 1974, pp. 269–289. doi:10.1016/0045-7825(74)90029-2

[26] Van Zante, Dale E., Strazisar, Anthony J., Wood, Jerry R., Hathaway, Michael D., and Okiishi, Theodore H., "Recommendations for Achieving Accurate Numerical Simulation of Tip Clearance Flows in Transonic Compressor Rotors," *Journal of Turbomachinery*, Vol. 122, Oct. 2000, pp. 733–742. doi:10.1115/1.1314609

[27] Menter, F. R., "Two-Equation Eddy-Viscosity Turbulence Models for Engineering Applications," *AIAA Journal*, Vol. 32, No. 8, 1994, pp. 1598–1605. doi:10.2514/3.12149

A. Prasad
Associate Editor